

Oriented Growth of Gold Nanowires on MoS₂

Daisuke Kiriya, Yuzhi Zhou, Christopher Nelson, Mark Hettick, Surabhi Rao Madhvapathy, Kevin Chen, Peida Zhao, Mahmut Tosun, Andrew M. Minor, Daryl C. Chrzan, and Ali Javey*

Layered 2D materials serve as a new class of substrates for templated synthesis of various nanomaterials even with highly dissimilar crystal structures; thus overcoming the lattice constraints of conventional epitaxial processes. Here, molybdenum disulfide (MoS₂) is used as a prototypical model substrate for oriented growth of in-plane Au nanowires (NWs) despite the nearly 8% lattice mismatch between MoS₂ and Au. Au NWs on the MoS₂ surface are oriented along three symmetrically equivalent directions within the substrate arising from the strong Au–S binding that templates the oriented growth. The kinetics of the growth process are explored through experiments and modeling. Strong charge transfer is observed between Au NWs and MoS₂, resulting in degenerate p-doping of MoS₂.

1. Introduction

The ability of one material to influence the crystallography of another at an interface is the foundation for constructing functional heterojunctions for a myriad of electronic, energy, and photonic applications. The ultimate limit of this process is epitaxy, whereby the second material, usually a thin layer, fully adopts the planar interface symmetry of the host substrate. Metal nanostructures with an epitaxial growth mode on semiconducting compounds^[1] and metal oxides^[2] have been

widely studied for use in catalytic,^[2a,b] plasmonic,^[1a,2d] and nanoelectronic^[1d,3] devices. Morphologies of the metal nanostructures should be taken into consideration to maximize the properties of the metal surface. In general, morphologies such as spheres (particles),^[1d,4] platelets (squares, triangles etc),^[1c,e] and vertically aligned pillars^[5] have been systematically generated. Since the interface of the junction is often a 2D crystalline plane with high symmetry, growth of anisotropic shapes, such as horizontal nanowires (NWs), on the plane can be difficult. Previously, in-plane oriented epitaxial growth of Si,^[6] metal oxide,^[7] and III–V NWs^[8]

have been demonstrated via the vapor–liquid–solid (VLS) process with metal nanoparticles as catalysts. In the conventional epitaxial growth process, the crystal structure and lattice constants of the substrates and grown material need to be closely matched. Here, we explore the use of layered materials as template substrates for oriented growth of in-plane metal NWs. As a proof of concept, we demonstrate growth of in-plane oriented Au NWs with C3 symmetry on molybdenum disulfide (MoS₂) surfaces. The rich surface chemistry of MoS₂ with weakly bonded layered structure facilitates the oriented growth of Au NWs despite the highly mismatched crystal structures of Au and MoS₂ with a large lattice mismatch of 8%. This work presents a unique platform for growth of highly dissimilar heterostructures using layered substrates; overcoming the lattice constraints of conventional epitaxial processes. Furthermore, we demonstrate degenerate p-doping of MoS₂ as a result of charge transfer with the Au NWs.

Transition metal dichalcogenides (TMDCs) are promising materials for the next generation electro-optical devices due to their atomically thin layered nature,^[9] variety of band gaps ranging from metallic to insulating depending on the combination of metals and chalcogenide atoms,^[10] relatively high carrier mobilities ($\approx 200 \text{ cm}^2 \text{ V}^{-1} \text{ s}^{-1}$ for WSe₂)^[11] and in some cases, high thermal and chemical stabilities^[10,12] for device fabrication processing. The bonding within each layer of TMDCs is ionic/covalent while the adjacent layers are coupled via van der Waals (vdW) interactions. Due to this weak interlayer binding and very smooth surface, vdW epitaxy has been proposed to form functional crystals on the surface of layered materials.^[13] Previously, vdW epitaxy of various 2D layered materials based on a combination of TMDCs, h-BN, and graphene has been reported.^[13a,14,15] Since the interaction with the substrate is not strong, the vdW epitaxy has mainly generated 2D symmetric crystals due to the laterally highly-symmetrical plane at the

Dr. D. Kiriya, M. Hettick, S. R. Madhvapathy,
K. Chen, P. Zhao, M. Tosun, Prof. A. Javey
Electrical Engineering and Computer Sciences
University of California
Berkeley, CA 94720, USA
E-mail: ajavey@berkeley.edu



Dr. D. Kiriya, Y. Zhou, M. Hettick, S. R. Madhvapathy,
K. Chen, P. Zhao, M. Tosun, Prof. D. C. Chrzan, Prof. A. Javey
Materials Sciences Division
Lawrence Berkeley National Laboratory
Berkeley, CA 94720, USA

Dr. D. Kiriya, M. Hettick, K. Chen, P. Zhao,
M. Tosun, Prof. A. Javey
Berkeley Sensor and Actuator Center
University of California
Berkeley, CA 94720, USA

Y. Zhou, Prof. A. M. Minor, Prof. D. C. Chrzan
Materials Science and Engineering
University of California
Berkeley, CA 94720, USA

Dr. C. Nelson, Prof. A. M. Minor
National Center for Electron Microscopy
Molecular Foundry
Lawrence Berkeley National Laboratory
Berkeley, CA 94720, USA

DOI: 10.1002/adfm.201502582

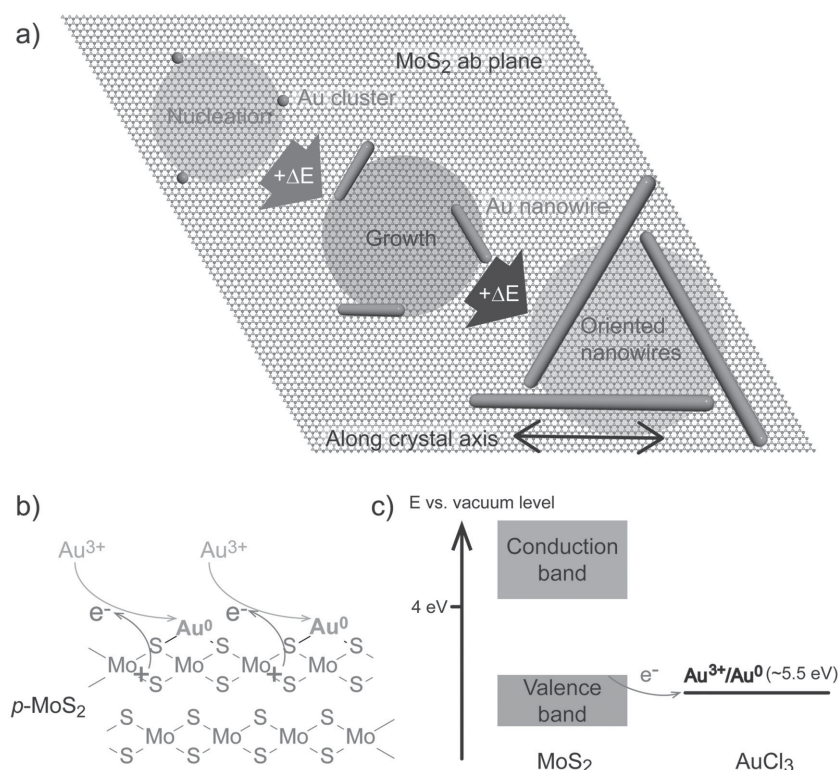


Figure 1. a) Schematic illustration of the growth of the in-plane oriented Au NWs on the MoS₂ surface. By casting AuCl₃ solution, Au atoms are supplied on the surface of MoS₂ (*ab* plane). Au atoms diffuse to form nuclei on the surface and eventually generate NWs by application of thermal energy. The NWs are in-plane oriented, reflecting the hexagonal lattice of the *ab* plane MoS₂. b) Schematic illustration of the redox reaction between Au³⁺ and MoS₂ to form an Au⁰-MoS₂ complex. c) Qualitative energy diagram between MoS₂ and AuCl₃. The reduction potential of Au³⁺/Au⁰ is ≈5.5 eV (vs vacuum level). Since the valence band edge of MoS₂ is less than ≈5.5 eV, electron transfer from MoS₂ to Au³⁺ occurs.

junction of the inorganic crystals.^[13,14] Here, we use MoS₂ as a model TMDC substrate to grow in-plane Au NWs despite the nearly 8% lattice mismatch between MoS₂ and Au. Au NWs on the MoS₂ surface are oriented along three symmetrically equivalent directions within the substrate arising from the strong Au-S binding that templates the oriented growth. A strong charge transfer reaction with MoS₂ is observed through electrical measurements, resulting in degenerate p-doping of MoS₂.

2. Results and Discussion

Figure 1a shows an illustrative image of the growth of Au NWs from nucleation to growth on the surface of MoS₂. Casting AuCl₃ solution onto MoS₂ supplies Au atoms on the surface. To form Au NWs on MoS₂, we cast a 30 wt% AuCl₃ solution in diluted HCl (Sigma-Aldrich) onto a mechanically exfoliated MoS₂ flake for 1 min and then blow off the extra solution with N₂ gas followed by annealing at 150 °C for 2 min on a hot plate in an ambient environment. During the thermal annealing process, Au atoms on the surface aggregate to form nuclei and further assemble to form NWs. Uniquely, the NWs are oriented with C₃ symmetry, suggesting coherence with the threefold symmetry^[10] of the surface of MoS₂. Previous works

have demonstrated self-assembled monolayers (SAM) of alkyl thiol molecules (R-SH) on Au surfaces.^[16] In the SAM case, a strong interaction between S and Au facilitates the formation of the monolayer of thiolate molecules on top of Au.^[16] The structure shown in Figure 1a is similar but opposite from the usual SAMs; Au atoms are instead assembled onto the S lattice of MoS₂. AuCl₃ was chosen as an Au source because it has a high reduction potential (≈5.5 eV vs vacuum level).^[17] With the valence band edge of MoS₂ less than ≈5.5 eV, a redox reaction between AuCl₃ and MoS₂ would occur spontaneously on the surface (Figure 1b,c) to supply Au atoms effectively.^[10b,17a] Previously, formation of Au nanoparticles on MoS₂ has been reported using a similar AuCl₃ treatment.^[1c,d,4,17a,18] Stimulated from the research, in-plane oriented Au NW formation was targeted in this research.

Figure 2a,b shows atomic force microscopy (AFM) images of a 6.4 nm thick MoS₂ flake before and after the AuCl₃ treatment, respectively. NWs are clearly observed on the surface after AuCl₃ treatment and thermal annealing. The length of the NWs is ≈500 nm with a diameter of ≈10 nm from the AFM observations. Since no NWs were observed on the surface of SiO₂ (Figure 2b), the growth of the NWs is expected to be controlled by the interaction between Au³⁺ and MoS₂. The NW formation is independent of MoS₂ flake thickness: NWs can also be formed on bilayers (1.5 nm thick, Figure 2c) and monolayers (0.7 nm thick, Figure 2d) of MoS₂. We analyzed the statistical distribution of the angles of the NWs shown in a 2.5 μm × 2.5 μm area (Figure 2d). We found that NWs were well oriented with peak distributions at approximately every 60°, along the ≈40°, 95°, and 154° directions, indicating the C₃ symmetry orientation (Figure 2e). Given the consideration of the C₃ symmetry of the *ab* plane of MoS₂ (Figure 1a) and no NW formation on the SiO₂ surface, the NW growth is strongly influenced from the MoS₂ substrate which is also suggested from the nuclei preferentially oriented along a lattice of MoS₂ (vide infra).

We further analyzed the effect of the AuCl₃ concentration and deposition time on NW morphology. Decreasing the concentration of AuCl₃ from 30 to 1 wt% by dilution with Milli-Q water decreases the diameter of NWs (*d*) from *d* = 17.5 nm (30 wt%) to *d* = 6.5 nm (1 wt%) (**Figure 3a–d** and **Figure S1**, Supporting Information) using the same deposition procedures as previously described (1 min deposition followed by 150 °C annealing for 2 min). Higher concentrations facilitate more Au deposition on the surface, leading to the generation of thicker Au NWs. We also found that there is a critical concentration for the generation of NWs based on the 1 min deposition procedure. Below 0.5 wt%, nanoparticles are formed instead (Figure 3e). However, by using a longer deposition time, even the 0.5 wt% AuCl₃ can be used to generate NWs (Figure 3f).

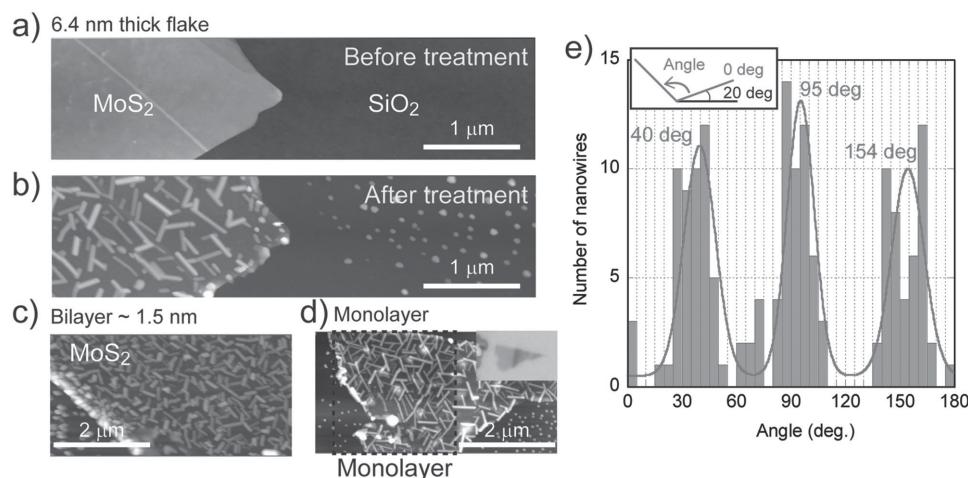


Figure 2. Demonstration of the oriented growth of Au NWs on MoS₂ surface. AFM images of an exfoliated MoS₂ flake (6.8 nm thickness) a) before and b) after Au NW growth on the surface. AFM images of Au NWs on c) bilayer and d) monolayer MoS₂. All samples were treated with a 30 wt% AuCl₃ solution followed by thermal annealing at 150 °C. e) Statistical distribution of the orientation angle of Au NWs on monolayer MoS₂ in (d). NWs are oriented at approximately every 60°. This orientation trend reflects the hexagonal symmetry of the MoS₂ *ab* surface. The histogram is fitted with three Gaussian distributions (red solid line).

This result also follows from the above discussion, indicating a critical amount of Au on MoS₂ needed to generate NWs. A longer deposition time of 60 min shows a similar distribution of Au NWs (≈ 10 nm thickness) as in the 10 min case (Figure 3g), indicating saturation of Au coverage on the MoS₂ surface by AuCl₃ treatment. Upon heating, these Au atoms diffuse and nucleate clusters. Higher concentrations lead to a higher nucleation rate for Au clusters. Faster growth rates are also expected for high concentration solutions.

Assembly of Au atoms on MoS₂ is found to show various morphologies from nanoparticles to NWs depending on the annealing conditions. Importantly, the NWs can be formed only in a limited annealing temperature condition. This is also observed under AFM before/after annealing of a MoS₂ flake treated with AuCl₃. Features were not observed before thermal annealing while on the other hand, NWs were clearly generated after annealing at 150 °C for 5 min (Figure S2, Supporting Information). Figure 4a shows a growth morphology diagram of Au on MoS₂ with various annealing times/temperatures. At the lower temperature region (below 100 °C), Au shows up only as small nanoparticles on MoS₂ (≈ 4 nm, Figure S3, Supporting Information). Increasing the temperature above 130 °C results in NW formation, suggesting that surface diffusion of Au is important to generate NWs (Figures S4 and S5, Supporting Information). With further annealing (either higher temperature or longer annealing time) the NWs display a pearling instability, and decompose into lines of Au nanoparticles (Figures S4–S6, Supporting Information). The above phase transformations are illustrated in Figure 4b. We speculate that after the deposition of AuCl₃ on MoS₂, both atomic Au and unreacted AuCl₃ molecules (*vide infra*) are present on the surface (Figure 4bi). Applying thermal energy ($\Delta E1$) to the complex induces diffusion of these species to form nuclei (nucleation, Figure 4bii). With increased annealing time/temperature and correspondingly, more thermal energy ($\Delta E2$), nucleation is completed and NWs are grown (Figure 4biii). More energy

($\Delta E3$) induces transformation of NWs into a sequence of nanoparticles and eventually coagulation of each nanoparticle to form a large particle by additional energy ($\Delta E4$). The observation of NW growth suggests an anisotropic growth rate along different Au crystalline facets. While the exact mechanism is intriguing and not well established, the presence of ions would play a critical role in the NW growth, similar to previously reported solution phase synthesis of NW growth.^[19] The importance of AuCl₃ existence on the MoS₂ surface is confirmed from a control experiment with evaporated Au (0 valence gold) that resulted in platelet structures instead of NWs after thermal annealing (Figure S7, Supporting Information). The C3 symmetry of the NW growth orientation suggests strong binding interaction between Au and S atoms on the surface of MoS₂. Thus, despite the different crystal structure and large lattice mismatch ($\approx 8\%$) of the two materials, the MoS₂ substrate acts as an effective template in guiding the orientation of the grown NWs on the surface.

The mechanism by which the MoS₂ substrate templates the growth process is not fully understood. Efforts to observe directly the relevant interface have been thwarted by the instability of the wires in the presence of an electron beam and/or light. When exposed to these forms of radiation, the NWs display a pearling instability and form Au clusters (as noted in Figure 4). One possible origin of the templating is that the wires are growing via vdW epitaxy.^[20] In this case, the growing wires would continue to feel the atomic scale corrugation of the substrate through the weak vdW bonding between the substrate and the wires, yielding a preferred orientation. Alternatively, more traditional epitaxy is also a possibility. As mentioned above, the lattice mismatch for {111} oriented growth is approximately 8% biaxially. (The lattice mismatch for {001} oriented growth would introduce lower, but still significant strain in the growing film.) Nevertheless, transmission electron microscopy (TEM) studies of the growth of Au on MoS₂, performed *in situ*, resulted in Au platelets that grew epitaxially on the substrate

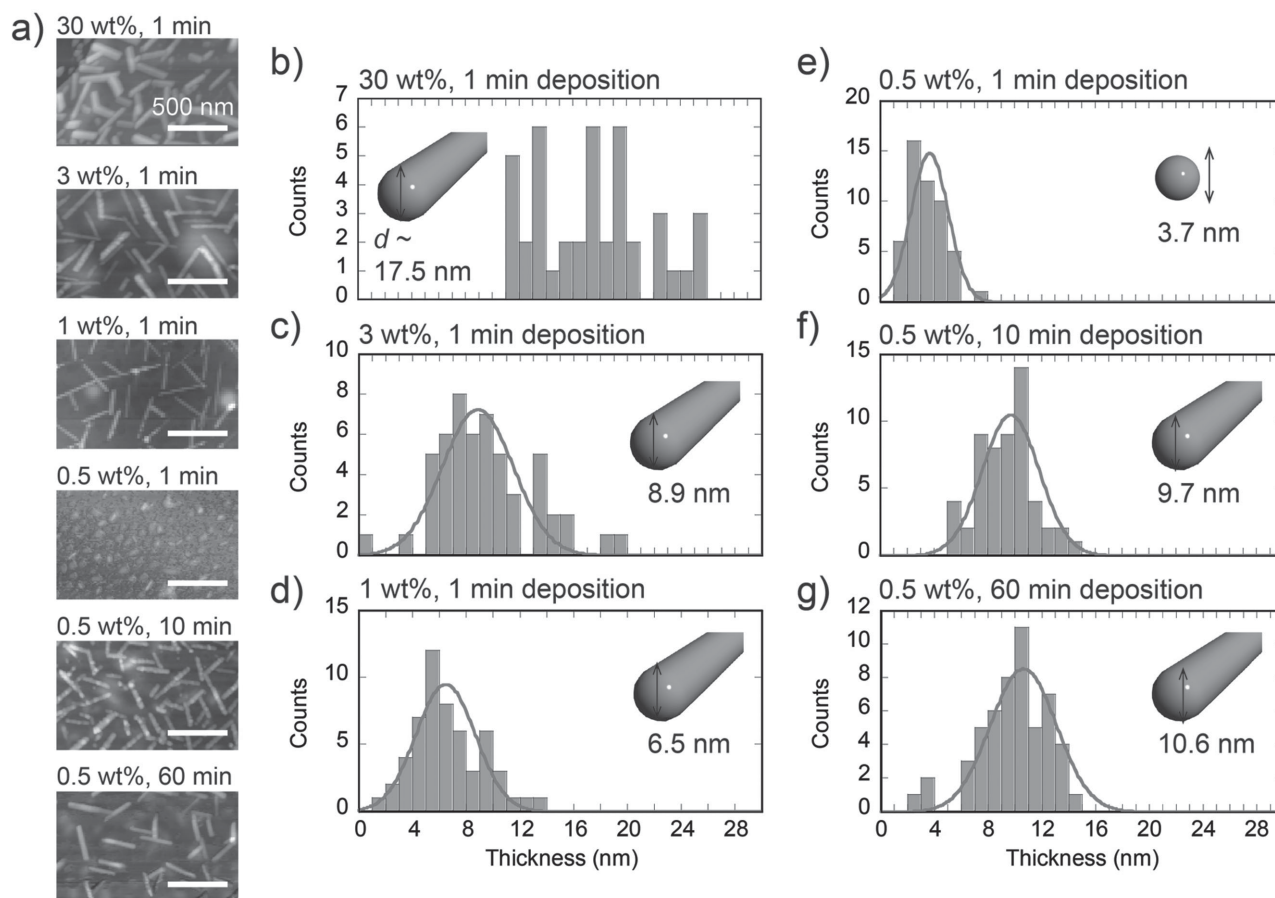


Figure 3. Concentration dependency of AuCl_3 on NW formation. a) AFM images of Au NWs/nanoparticles on MoS_2 obtained from treatment with various AuCl_3 concentrations followed by thermal annealing at 150°C for 2 min. Concentrations and deposition times are labeled above each image. b–g) Histograms of the diameter of Au nanostructures obtained from AuCl_3 depositions with b) 30 wt% for 1 min, c) 3 wt% for 1 min, d) 1 wt% for 1 min, e) 0.5 wt% for 1 min, f) 0.5 wt% for 10 min, and g) 0.5 wt% for 60 min. Except for the case of 0.5 wt% for 1 min, all other conditions result in the formation of NWs. Red solid lines in the histograms are Gaussian fitting lines. In the case of the 30 wt% for 1 min case, the fitting failed due to the high dispersity.

(most likely with the introduction of misfit dislocations).^[21] A recent theoretical analysis suggests that $\{111\}$ oriented epitaxy is favored by the strength of the Au–S bond at the interface, and the elastic compliance of the MoS_2 substrate.^[22] Similar factors could be influencing the growth of the NWs, and an epitaxial relationship would help to explain the preferred growth direction.

To characterize the state of the Au clusters on MoS_2 , we carried out X-ray photoelectron spectroscopy (XPS) analysis (Figure 5a,b). Figure 5a presents Au core levels ($4f$) from the treatment with 30 wt% AuCl_3 solution followed by thermal annealing as shown in Figure 2. The four peaks observed correspond to Au^{3+} and Au^0 doublets, with both $4f_{7/2}$ and the indicated $4f_{5/2}$ components fit as Voigt lineshapes.^[23] The peak area ratio corresponding to $4f_{5/2}$ of Au^{3+} to Au^0 is $\approx 23\%$. This suggests that close to 80% of the Au^{3+} is converted into Au^0 on the MoS_2 surface, indicating strong electron transfer between MoS_2 and Au^{3+} . Figure 5b indicates the core levels of Cl ($2p$) on the same sample. Two types of Cl species are observed, corresponding to Cl–Au species originating in $[\text{AuCl}_4]^-$ and Cl atoms on MoS_2 which would be in the form of Cl^- ions.^[23,24] From the

relative area of each Cl core level peak, we estimate $\approx 30\%$ of the total Cl atoms are Cl^- ions on MoS_2 . According to these results, the surface is mostly coated with elemental Au clusters with measurable $[\text{AuCl}_4]^-$ content. The X-ray diffraction (XRD) analysis in Figure S8 (Supporting Information) further identifies the assembly of crystalline Au on MoS_2 after AuCl_3 treatment and annealing.

The preferential crystallographic alignment of some of the Au nanoparticle nuclei prior to Au NW growth was observed by selected area electron diffraction (SAED) using TEM (Figure S9, Supporting Information). SAED diffraction patterns were taken from multiple Au nanoparticles on a free-standing MoS_2 flake and exhibited diffraction peaks consistent with d -spacings of the bulk Au fcc phase. A consistent preferred orientation was not apparent for this sample size (≈ 20 particles), but aligned diffraction peaks were observed for $\text{Au}\{220\}||\text{MoS}_2(\bar{1}\bar{1}0)$, $\text{Au}\{311\}||\text{MoS}_2(\bar{2}10)$, $\text{Au}\{111\}||\text{MoS}_2(100)$, and $\text{Au}\{200\}||\text{MoS}_2(310)$. Given the variety of observed orientations and noting that not all particles in the set had visible diffraction peaks nor did any appear to share a principle zone axis with MoS_2 , the MoS_2 surface in the TEM study did not

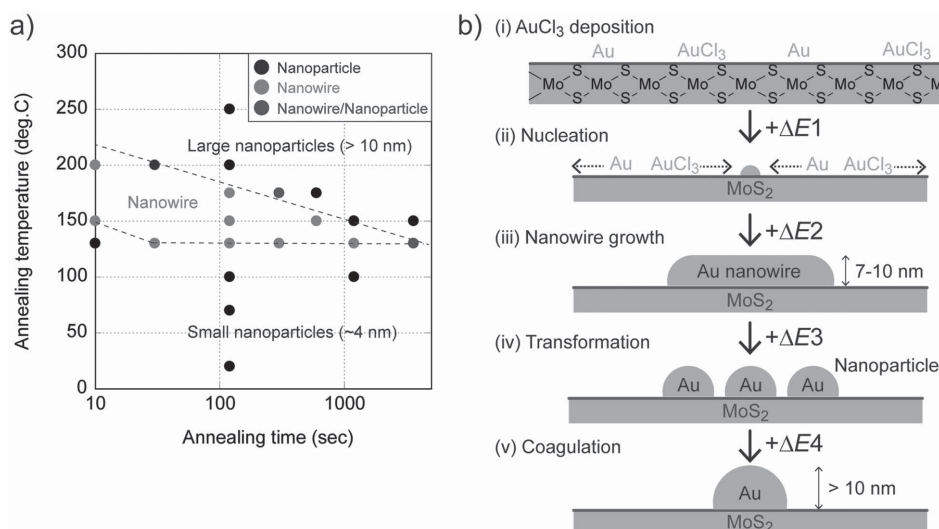


Figure 4. a) Growth morphology diagram of Au nanostructures on MoS₂ as a function of annealing time and temperature (with a 3 wt% AuCl₃ solution casted for 1 min). NWs are generated in a limited range (temperatures between 130 to 200 °C and annealing time below 1 h). b) Plausible transformation of Au nanostructures on MoS₂ as a function of thermal energy. i) Casting of AuCl₃ solution on MoS₂ supplies Au on MoS₂. Applying additional energy ($\Delta E1$ to $\Delta E4$) induces ii) nucleation from Au atoms by $\Delta E1$, iii) nanowire generation by $\Delta E2$, iv) a transformation of NWs into a set of nanoparticles by $\Delta E3$, and v) coagulation of nanoparticles into large particles by $\Delta E4$.

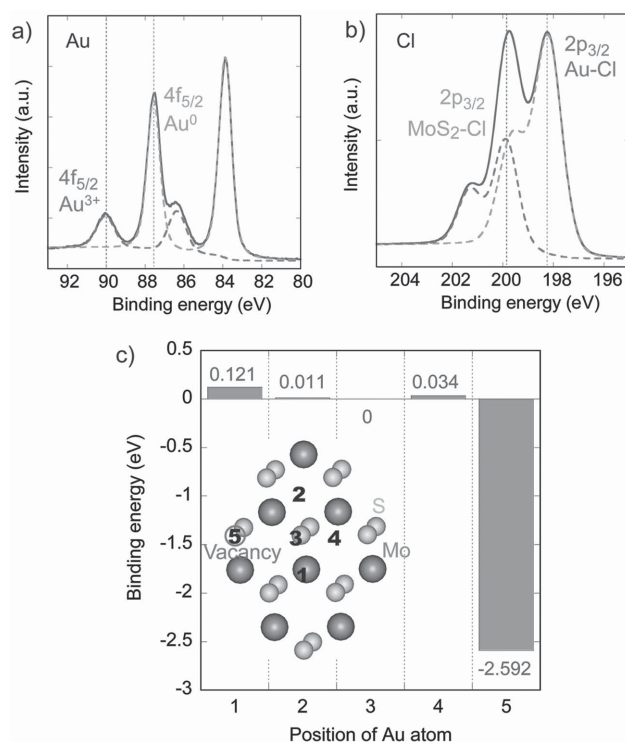


Figure 5. Characterization of Au on MoS₂. XPS spectra for a) Au core levels (4f_{7/2} and 4f_{5/2}) and b) Cl core levels (2p_{3/2} and 2p_{1/2}) for an MoS₂ sample after treatment with a 30 wt% AuCl₃ for 1 min followed by annealing at 150 °C for 2 min. c) Relative binding energy obtained from DFT simulations for an Au atom on various MoS₂ positions. The energy for the Au on S atom of MoS₂ is set as 0 eV. Each position is defined as follows: 1: Au on top of Mo; 2: Au on an interstitial site of the hexagonal lattice; 3: Au on S; 4: Au on an interstitial site between two S atoms; and 5: Au on S vacancy.

appear to strongly enforce a crystallographic orientation of the Au nuclei. However, wherever the gold planes were visible by SAED they exhibited preferential orientation to a nearby MoS₂ plane. Unfortunately, a similar TEM study of NWs could not be performed due to pearling instability of the wires under the electron beam converting the NWs into nanoparticles.

Theoretical simulation using density functional theory (DFT) was also applied to better understand the nucleation from the interaction between Au atom and MoS₂ on the surface (Figure 5c and Supporting information). Compared to Au atom on the S atom of MoS₂, Au atom on the Mo atom of MoS₂ shows a higher energy (0.12 eV). The result is as expected; Au and S atoms have higher affinity. Another important point is that the binding energy of Au atom on S vacancies was found to be -2.6 eV. This interaction is found to be thermodynamically very strong, which would be the main nucleation site for Au clusters.

To analyze the electrical properties of MoS₂ after the generation of Au NWs, we examined the transfer characteristics of back gated MoS₂ field-effect transistors (FETs). FETs were fabricated by mechanically exfoliating ≈ 100 nm thick MoS₂ flakes on 260 nm SiO₂ on a heavily doped p⁺-Si wafer as a universal back gate (Figure 6a,b). Photolithography is used to define source and drain electrodes followed by evaporation of Au/Cr (40/0.5 nm). The channel length of the devices is 10 μ m. Figure 6a and Figure S10 (Supporting Information) show transfer characteristic curves (drain voltage (V_{DS}) = +1 or -1 V for n and p type characteristics, respectively) before/after treatment of 1 wt% AuCl₃ on the device. The pristine device shows n-type behavior as similar to previous reports. After the treatment of the AuCl₃, the polarity of the device changes from n-type to p-type and the ON current level monotonically increases several orders of magnitude ($\approx 10^3$) with increasing deposition time of the AuCl₃. Previously, a report demonstrated

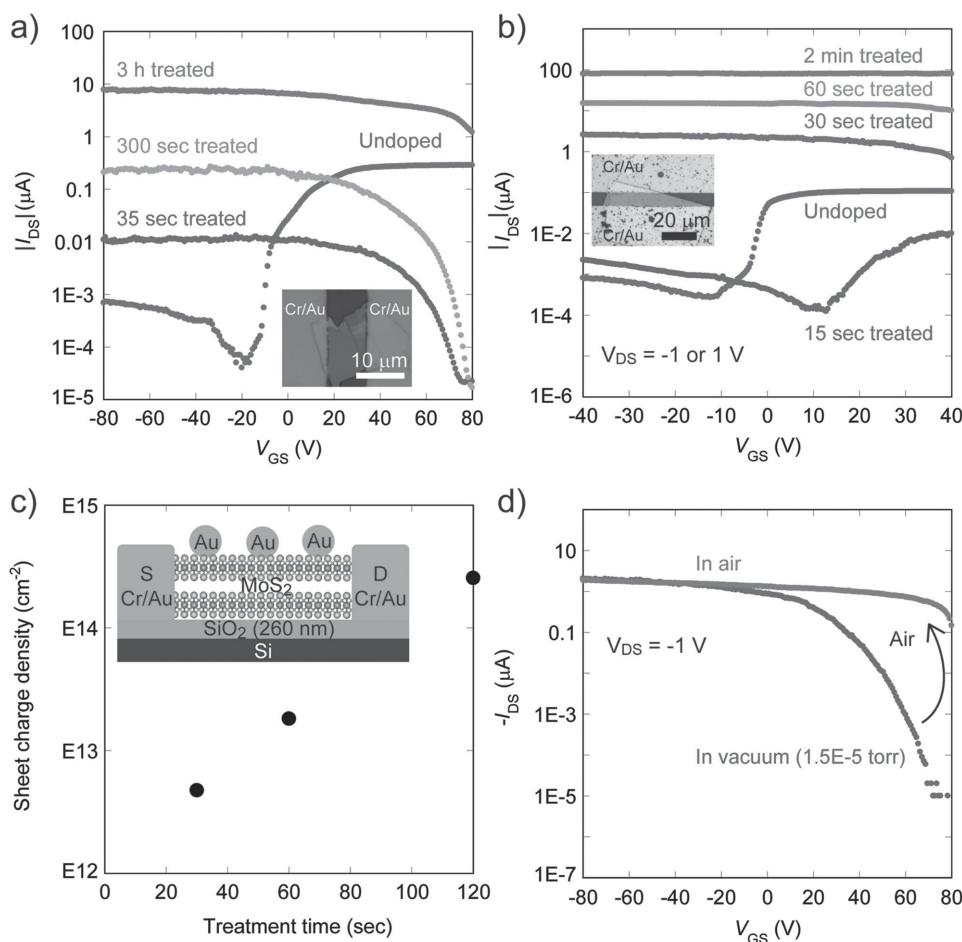


Figure 6. Electrical characterization of MoS₂ after Au NW growth. a) Characteristic transfer curves after each sequential treatment (1 wt% AuCl₃ solution followed by annealing at 150 °C for 2 min each) for a device with 95 nm thick MoS₂. The pristine MoS₂ shows n-type behavior and adding the treatment (from 35 s to 3 h) switches the polarity and increases the ON current level. Inset shows an optical microscope image of the device used for this experiment. V_{DS} = +1 or –1 V for before and after AuCl₃ treatment, respectively. b) A similar treatment study as shown in Figure 6a using a 30 wt% AuCl₃ solution and an MoS₂ flake with 114 nm thickness. c) Sheet hole density in the Au decorated MoS₂ devices as a function of AuCl₃ deposition time. The charge density monotonically increases with the AuCl₃ deposition time to 2.5 × 10¹⁴ cm^{–2} after 2 min. d) Environmental effect on the doping of MoS₂ by Au NWs. The thickness of the flake is 29 nm. When placed in ≈10^{–5} Torr vacuum, the transfer characteristic curve shows strong gate dependency with ON/OFF ≈ 10⁵ (blue curve) arising from reduced doping. After reexposure to air, the curve goes back to the degenerately doped state with no gate dependency (red curve). The ambient effect arises from the known sensitivity of the Au work function to H₂O and O₂.

AuCl₃ can act as an acceptor; the polarity transformation in our case is comparable.^[25] As discussed in Figure 3e,f, since a longer deposition time increases the surface coverage of Au on MoS₂, the hole concentration of MoS₂ is also increased as the deposition time increases. Interestingly, in the case of using 30 wt% AuCl₃ solution (Figure 6b), just a 30 s treatment shows a drastic change in the electrical properties, resulting in small V_{GS} dependency, corresponding to a degenerately doped p⁺ situation. Treatments longer than 30 s increase I_{DS} monotonically. From these characteristic curves, we extracted the sheet charge density (n_{2D}) using the Equation (1).^[26]

$$n_{2D} = (I_{DS}L) / (qWV_{DS}\mu) \quad (1)$$

where q is the electron charge, W and L represent width and length of the channel, respectively, I_{DS} is the drain current at V_{GS} = 0 V, V_{DS} is the source to drain bias, and μ is the

field-effect hole mobility. We used $W = 45 \mu\text{m}$ by averaging the width of the two source and drain metal contacts. As shown in Figure 6c, the carrier density increases with increasing doping time to 2.5 × 10¹⁴ cm^{–2} at 120 s. Previously, NO₂ was used as a p-type degenerate dopant for WSe₂, with a doping concentration ceiling of ≈ 10¹³ cm^{–2}.^[11] The growth of Au on the surface of MoS₂ also induces the high carrier concentration due to its effective surface charge transfer interaction.

When measured under vacuum (≈10^{–5} Torr), the degenerate p-doped state of Au doped MoS₂ converts into a nondegenerate state with an ON/OFF ratio over 10⁵ (Figure 6d). A reexposure of the device back to ambient environment immediately reverses the transfer characteristic back to a representative p⁺-type degenerate state without gate dependency. From these results, we attribute work function modulation of the Au due to air adsorbates as responsible for the demonstrated reversible transfer characteristic between the degenerate state and

nondegenerate states. Previously, devices with carbon nanotubes (CNTs) as a channel material showed similar reversible transfer characteristics.^[27] The work function of Au is easily affected by adsorbates such as water and oxygen, and in our case, these adsorbates would change the work function of the Au NWs (and nanoparticles) on MoS₂.^[28] As a control experiment, since the solution of AuCl₃ is HCl-based, we examined a similar back gated MoS₂ device treated with HCl only (Figure S11, Supporting Information). Although the ON current level was increased by annealing due to changes in the metal contact, the polarity of MoS₂ was maintained to be *n*-type, signaling the doping is due to the AuCl₃ and not the HCl.

3. Conclusions

In summary, we demonstrate in-plane oriented growth of Au NWs with C3 symmetry on layered MoS₂ substrates by deposition of AuCl₃ solutions and thermal annealing. Despite the large difference in the crystal structure of the two materials, MoS₂ surface serves as an effective template substrate in guiding the oriented growth of Au NWs. Preliminary theoretical studies suggest the process is facilitated by the layered structure of MoS₂ which allows for mechanical compliance of its top surface layer, and the strong S–Au binding. The work suggests a new crystal growth platform by using layered substrates to overcome the crystal lattice constraints of conventional epitaxial processes.

4. Experimental Section

Fabrication of the Devices: The devices shown in Figure 6 were fabricated via standard photolithographic techniques. Source and drain metal pads (Cr/Au = 0.5/40 nm) were made via electron beam evaporation followed by lift-off.

Treatment of AuCl₃ onto MoS₂: The preparation of Au NWs was done with the following procedures. First, MoS₂ flakes were exfoliated via mechanical exfoliation onto an Si wafer with 260 nm of thermal oxide. AuCl₃ solution (AuCl₃ in HCl, Sigma Aldrich) was then dropcast onto the MoS₂ flake and subsequently blown off with dry N₂ gas. Finally, the sample was annealed at 150 °C for several minutes (usually 2 min). The test of AuCl₃ concentrations ranged from 0.5 to 30 wt%, diluted with Milli-Q water from an original concentration of 30 wt%. For electrical measurements (Figure 6), the AuCl₃ treatment was done after fabrication of the back gated devices.

Supporting Information

Supporting Information is available from the Wiley Online Library or from the author.

Acknowledgements

This work was supported by the Director, Office of Science, Office of Basic Energy Sciences, Material Sciences and Engineering Division of the US Department of Energy under Contract No. DE-AC02-05CH11231. The device fabrication and characterization was funded by the Center for Low Energy Systems Technology (LEAST), one of six centers supported by the STARnet phase of the Focus Center Research Program (FCRP),

a Semiconductor Research Corporation program sponsored by MARCO and DARPA. The transmission electron microscopy and XRD were performed at the Molecular Foundry, supported by the Office of Science, Office of Basic Energy Sciences, of the U.S. Department of Energy under Contract No. DE-AC02-05CH11231. XPS characterization was performed at the Joint Center for Artificial Photosynthesis, supported through the Office of Science of the US Department of Energy under Award Number DE-SC0004993.

Received: June 23, 2015

Revised: August 13, 2015

Published online: September 16, 2015

- [1] a) Y. J. Lu, J. Kim, H. Y. Chen, C. H. Wu, N. Dabidian, C. E. Sanders, C. Y. Wang, M. Y. Lu, B. H. Li, X. G. Qiu, W. H. Chang, L. J. Chen, G. Shvets, C. K. Shih, S. Gwo, *Science* **2012**, 337, 450; b) W. L. Shi, H. Zeng, Y. Sahoo, T. Y. Ohulchanskyy, Y. Ding, Z. L. Wang, M. Swihart, P. N. Prasad, *Nano Lett.* **2006**, 6, 875; c) X. Huang, Z. Y. Zeng, S. Y. Bao, M. F. Wang, X. Y. Qi, Z. X. Fan, H. Zhang, *Nat. Commun.* **2013**, 4, 4; d) Y. M. Shi, J. K. Huang, L. M. Jin, Y. T. Hsu, S. F. Yu, L. J. Li, H. Y. Yang, *Sci. Rep.* **2013**, 3; e) G. Honjo, K. Yagi, *J. Vac. Sci. Technol.* **1969**, 6, 576.
- [2] a) V. Komanicky, H. Iddir, K. C. Chang, A. Menzel, G. Karapetrov, D. Hennessy, P. Zapol, H. You, *J. Am. Chem. Soc.* **2009**, 131, 5732; b) C. Wang, H. Daimon, S. H. Sun, *Nano Lett.* **2009**, 9, 1493; c) F. R. Fan, Y. Ding, D. Y. Liu, Z. Q. Tian, Z. L. Wang, *J. Am. Chem. Soc.* **2009**, 131, 12036; d) Z. X. Chen, B. Y. Lai, J. M. Zhang, G. P. Wang, S. Chu, *Nanotechnology*, **2014**, 25.
- [3] a) J. Schornbaum, B. Winter, S. P. Schiessl, F. Gannott, G. Katsukis, D. M. Guldi, E. Spiecker, J. Zaumseil, *Adv. Funct. Mater.* **2014**, 24, 5798; b) C. H. Lee, T. Schiros, E. J. G. Santos, B. Kim, K. G. Yager, S. J. Kang, S. Lee, J. Yu, K. Watanabe, T. Taniguchi, J. Hone, E. Kaxiras, C. Nuckolls, P. Kim, *Adv. Mater.* **2014**, 26, 2812.
- [4] L. H. Yuwen, F. Xu, B. Xue, Z. M. Luo, Q. Zhang, B. Q. Bao, S. Su, L. X. Weng, W. Huang, L. H. Wang, *Nanoscale* **2014**, 6, 5762.
- [5] a) R. S. Wagner, W. C. Ellis, *Appl. Phys. Lett.* **1964**, 4, 89; b) P. D. Yang, H. Q. Yan, S. Mao, R. Russo, J. Johnson, R. Saykally, N. Morris, J. Pham, R. R. He, H. J. Choi, *Adv. Funct. Mater.* **2002**, 12, 323.
- [6] L. W. Yu, M. K. Xu, J. Xu, Z. G. Xue, Z. Fan, G. Picardi, F. Fortuna, J. Z. Wang, J. Xu, Y. Shi, K. J. Chen, P. R. I. Cabarrocas, *Nano Lett.* **2014**, 14, 6469.
- [7] D. Tsvion, M. Schvartzman, R. Popovitz-Biro, E. Joselevich, *ACS Nano* **2012**, 6, 6433.
- [8] a) D. Tsvion, M. Schvartzman, R. Popovitz-Biro, P. von Huth, E. Joselevich, *Science* **2011**, 333, 1003; b) S. A. Fortuna, J. G. Wen, I. S. Chun, X. L. Li, *Nano Lett.* **2008**, 8, 4421.
- [9] Y. Yoon, K. Ganapathi, S. Salahuddin, *Nano Lett.* **2011**, 11, 3768.
- [10] a) M. Chhowalla, H. S. Shin, G. Eda, L. J. Li, K. P. Loh, H. Zhang, *Nat. Chem.* **2013**, 5, 263; b) M. Tosun, D. Fu, S. B. Desai, C. Ko, J. S. Kang, D.-H. Lien, M. Najmzadeh, S. Tongay, J. Wu, A. Javey, *Sci. Rep.* **2015**, 5, 10990.
- [11] H. Fang, S. Chuang, T. C. Chang, K. Takei, T. Takahashi, A. Javey, *Nano Lett.* **2012**, 12, 3788.
- [12] B. Radisavljevic, A. Radenovic, J. Brivio, V. Giacometti, A. Kis, *Nat. Nanotechnol.* **2011**, 6, 147.
- [13] a) Y. J. Hong, W. H. Lee, Y. P. Wu, R. S. Ruoff, T. Fukui, *Nano Lett.* **2012**, 12, 1431; b) H. Oh, Y. J. Hong, K. S. Kim, S. Yoon, H. Baek, S. H. Kang, Y. K. Kwon, M. Kim, G. C. Yi, *NPG Asia Mater.* **2014**, 6, e145.
- [14] a) H. Ago, H. Endo, P. Solís-Fernández, R. Takizawa, Y. Ohta, Y. Fujita, K. Yamamoto, M. Tsuji, *ACS Appl. Mater. Int.* **2015**, 7, 5265; b) Y. M. Shi, W. Zhou, A. Y. Lu, W. J. Fang, Y. H. Lee, A. L. Hsu, S. M. Kim, K. K. Kim, H. Y. Yang, L. J. Li, J. C. Idrobo,

- J. Kong, *Nano Lett.* **2012**, 12, 2784; c) P. K. Mohseni, A. Behnam, J. D. Wood, C. D. English, J. W. Lyding, E. Pop, X. L. Li, *Nano Lett.* **2013**, 13, 1153.
- [15] W. C. Lee, K. Kim, J. Park, J. Koo, H. Y. Jeong, H. Lee, D. A. Weitz, A. Zettl, S. Takeuchi, *Nat. Nanotechnol.* **2015**, 10, 423.
- [16] a) H. Häkkinen, *Nat. Chem.* **2012**, 4, 443; b) W. S. Liao, S. Cheunkar, H. H. Cao, H. R. Bednar, P. S. Weiss, A. M. Andrews, *Science*, **2012**, 337, 1517.
- [17] a) J. Kim, S. Byun, A. J. Smith, J. Yu, J. X. Huang, *J. Phys. Chem. Lett.* **2013**, 4, 1227; b) K. K. Kim, J. J. Bae, H. K. Park, S. M. Kim, H. Z. Geng, K. A. Park, H. J. Shin, S. M. Yoon, A. Benayad, J. Y. Choi, Y. H. Lee, *J. Am. Chem. Soc.* **2008**, 130, 12757.
- [18] a) T. S. Sreeprasad, P. Nguyen, N. Kim, V. Berry, *Nano Lett.* **2013**, 13, 4434; b) S. Su, H. F. Sun, F. Xu, L. H. Yuwen, L. H. Wang, *Electroanal.* **2013**, 25, 2523.
- [19] Y. N. Xia, Y. J. Xiong, B. Lim, S. E. Skrabalak, *Angew. Chem. Int. Ed.* **2009**, 48, 60.
- [20] A. Koma, *Thin Solid Films* **1992**, 216, 72.
- [21] D. W. Pashley, M. J. Stowell, M. H. Jacobs, T. J. Law, *Philos. Mag.* **1964**, 10, 127.
- [22] Y. Zhou, D. Kiriya, E. E. Haller, J. W. Ager, A. Javey, D. C. Chrzan, arXiv:1505.07505, **2015**.
- [23] S. M. Kim, K. K. Kim, Y. W. Jo, M. H. Park, S. J. Chae, D. L. Duong, C. W. Yang, J. Kong, Y. H. Lee, *ACS Nano* **2011**, 5, 1236.
- [24] S. Jung, J. T. Han, J. S. Woo, J. H. Kim, H. J. Jeong, G. W. Lee, *Nanoscale* **2014**, 6, 2971.
- [25] M. S. Choi, D. Qu, D. Lee, X. Liu, K. Watanabe, T. Taniguchi, W. J. Yoo, *ACS Nano*, **2014**, 8, 9332.
- [26] H. Fang, M. Tosun, G. Seol, T. C. Chang, K. Takei, J. Guo, A. Javey, *Nano Lett.* **2013**, 13, 1991.
- [27] I. Lee, U. J. Kim, H. Bin Son, S. M. Yoon, F. Yao, W. J. Yu, D. L. Duong, J. Y. Choi, J. M. Kim, E. H. Lee, Y. H. Lee, *J. Phys. Chem. C* **2010**, 114, 11618.
- [28] R. L. Wells, T. Fort, *Surf. Sci.* **1972**, 32, 554.